Open Access Journal

Journal of Sustainable Research in Engineering Vol. 8 (1) 2024, 1-16

Journal homepage: http://sri.jkuat.ac.ke/ojs/index.php/sri

Influence of major biodiesel components on soot formation in biodiesel co-flow jet flames

R. M. Kiraithe[1], J. K. Tanui[1]*, P. N. Kioni[1]

[1]*Department of Mechanical Engineering, Dedan Kimathi University of Technology Private Bag, 10143, Dedan Kimathi, Nyeri, Kenya*

[*]*Corresponding Author - E-mail: josephat.tanui@dkut.ac.ke*

Abstract Soot formation in biodiesel combustion was studied by focusing on the major components in isolation. The aim of the study was to establish the influence of major components on soot production in combustion of biodiesel in co-flow jet flames. The components investigated in this study were methyl linolenate (MLe), methyl stearate (MS), methyl oleate (MO), methyl linoleate (MLi) and methyl palmitate (MP). The study was based on Moss-Brooke's soot model. A reduced kinetic mechanism for the pyrolysis and combustion of biodiesel surrogates with 177 chemical species and 2904 chemical reactions was implemented. Nucleation rate, coagulation rate, oxidation rate and soot volume fraction were investigated under laminar flow conditions. It was established that unsaturated methyl esters had higher soot formation rates than their saturated counterparts. MLe had the greatest influence in soot formation due to its relatively higher nucleation, coagulation and oxidation rates while MS had the least at the same boundary conditions. Analysis of the flame structure reveals that the higher nucleation rates are correlated to higher content of aromatic species in the immediate chemical reactions.

Keywords: Soot formation, biodiesel, methyl esters, soot model, jet flame, co-flow.

1. Introduction

Biodiesel is one of the fuels that is used as an alternative to fossils-based fuels. It is produced from renewable biological materials and doesn't contribute to increase of carbon dioxide (CO_2) in the atmosphere [1]. Biodiesel consists of unsaturated and saturated esters. The five major components are methyl palmitate (MP), methyl stearate (MS), methyl oleate (MO), methyl linolenate (MLe), and methyl linoleate (MLi), whose proportions vary depending on the kind of biodiesel fuel [2]. Different compositions found in biodiesels are as a result of different origins of feedstock and production region.

Combustion of biodiesel produces pollutants: Soot, CO_2 and Nitrogen oxides (NO_x). Thus, combustion devices for biodiesel fuels require optimization to reduce the amount of these pollutants [3]. Soot is one of the major products produced during incomplete combustion of hydrocarbon fuels. Soot is a lattice-like particulate debris that arises due to unburnt hydrocarbon. Soot production during combustion reduces the thermal efficiency of combustion devices, and affects the environment as well as human health [4, 5]. Soot formation indicates poor burning conditions, and that the fuel was not fully oxidized to carbon dioxide and water for the highest energy realization.

Soot accounts for 50–80 % of the particulate matter [6] produced during incomplete combustion of hydrocarbon [7]. Carbon, which is the main component of soot, forms the final matter by absorbing metal and organic matters [3]. Soot formation process consists of a complex chemical process (gas-phase process) and physical process (soot particle dynamics). The process begins with pyrolysis and oxidation, and then combination and cyclization reactions which result in formation of polycyclic aromatic hydrocarbons (PAHs). PAHs undergo nucleation as it continues to grow and form the inception of soot. After nucleation, the primary soot particles undergo congealing and surface development [8]. Surface growth comprises PAHs condensation. Such growth is responsible for an increase of soot particle size

and mass [4]. Primary particles collide to form chain-like particle aggregates. Since the soot generated is at elevated temperatures, the soot formation is continually accompanied by oxidation. O_2 and OH radicals play an important role in oxidation [9] .

There are several studies on soot formation in biodiesel fuel combustion. Gao *et al.* [10] investigated the effects of addition of dibutyl ether to biodiesel surrogates on co-flow flames using a laser-induced incandescence technique. Dibutyl ether mole fraction in the fuel stream was varied from 0 to 40 mol %. 2D soot volume fraction distribution was used to analyze the soot formation. The authors reported that, addition of dibutyl ether reduced yielding of soot. Soot reduction with more dibutyl ether addition was attributed to lower rate of nucleation and declining PAHs condensation. Moderate soot in flame wings was a result of competition between the declining percentage of inception and improved surface growth triggered by advanced concentration of acetylene. Chong *et al.* [11] investigated on quantification of carbon particulates under pool and prevaporised diffusion jet flame on blends of diesel and waste cooking oil biodiesel using laser induced-incandescence. The soot volume fraction of waste cooking oil biodiesel and blends was quantified and compared under the similar carbon flow rate through prevaporised jet flames and pool flames. The study established that the distribution of spatial soot volume fraction for diesel-rich fuels peaked near the flame and then convected downstream while biodiesel flames produced an evenly distributed soot volume proportion at the center of the flame. Biodiesel increase in the blend resulted in reduced soot propensity in both vaporized and pool flames. The reduction in soot propensity is due to lower content of aromatic species (mono-aromatics) [12].

Chong and Hochgreb *et al.* [13] investigated spray combustion of sunflower biodiesel and diesel fuel using swirl burner via twin-fluid atomizer-swirler arrangement. The study reported that bluish flame wings were observed in biodiesel flames as compared to sooty diesel flame wings. The bluish flame wings observed in biodiesel flames are attributed to relatively lower soot inception near the wing region as compared to diesel flames. Chiong *et al.* [14] study on combustion of palm, coconut and soybean biodiesel under spray flame using an air blast-type nozzle with air-to-liquid ratio variation, showed that biodiesel under lean conditions exhibited bluish spray flame without yellowish soot brush due to complete combustion. The authors also reported lower soot formation in biodiesel combustion as compared to diesel flames [15]. Biodiesel is inherently oxygenated which is responsible for less soot formation tendency. The oxygen presence in biodiesel helps in soot oxidation, hence reducing the particles surface growth. Additionally, esters molecules present in biodiesel reduce the concentration of ethylene (C_2H_4),which is responsible in the formation of acetylene (C_2H_2) species as soot precursor [16].

Compared to diesel there is reduced soot formation in combustion of biodiesel. However, the extent of soot formation in biodiesel varies considerably depending on the feedstock used in the production of biodiesel. The feedstock methyl esters composition. For example, canola oil biodiesel has 11.1 % MLe, 21.1 % MLi, 60.2 % MO, 3.7 % MP and 3.9 % MS while palm oil biodiesel has 0.4 % MLe, 53.14 % MLi, 18.93 % MO, 24.90 % MP and 2.63 % MS [17]. The exact contribution from each methyl ester component to the overall soot formation in biodiesel is still not clear. Therefore, it is important to establish how different methyl esters in biodiesel affect the overall soot generation during biodiesel combustion. Previous studies have concentrated on soot formation in biodiesel and biodiesel blend flames. Since methyl esters concentration varies across biodiesel types, this study focuses on establishing the influence of major methyl esters by studying them in isolation. Studying soot formation of the individual methyl esters in isolation is a way of determining their effect on the overall soot formation in the aggregate biodiesel fuel. This study focused on the major biodiesel methyl esters: methyl linolenate ($C_{19}H_{32}O_2$), methyl stearate ($C_{19}H_{38}O_2$), methyl oleate ($C_{19}H_{36}O_2$), methyl linoleate ($C_{19}H_{34}O_2$) and methyl palmitate ($C_{17}H_{34}O_2$). These major esters have varying numbers of carbon double bonds and the relative concentration of carbon atoms they possess.

2. Material and Methods

The paper reports numerical simulation of soot formation. The Moss-Brookes semi-empirical model is adopted since it gives better insights on soot formation mechanism. Moss-Brookes model was employed in this study to determine the nucleation rates, surface growth rates, coagulation rates and soot volume fraction.

2.1 Governing Equations

The governing equations applied in this study are those for laminar flow in a 2-D axisymmetric co-flow configuration. The independent variables are the distances Z from the inlet along the axis and *r* from the center. The dependent variables of interest are the axial

and radial velocity u and v, density ρ, pressure p, temperature T and mass fraction Y_i, I = 1, 2, ..., N. The system of governing equations consists of conservation equations for mass, momentum, species, energy and state equation as represented by Eqs. (1) – (6) [18,19].

Mass conservation;

$$\frac{1}{r}\frac{\partial}{\partial r}(r\rho u) + \frac{\partial}{\partial Z}(\rho u) = 0 \quad (1)$$

Momentum equations;

Axial component;

$$\rho v\frac{\partial u}{\partial r} + \rho u\frac{\partial u}{\partial r} = -\frac{\partial p}{\partial Z} + \frac{1}{r}\frac{\partial}{\partial r}\left(r\mu\frac{\partial u}{\partial r}\right) + 2\frac{\partial}{\partial Z}\left(\mu\frac{\partial u}{\partial Z}\right) - \frac{2}{3}\frac{\partial}{\partial Z}\left[\frac{\mu}{r}\frac{\partial u}{\partial r}rv\right] - \frac{2}{3}\frac{\partial}{\partial Z}\left(\mu\frac{\partial u}{\partial Z}\right) + \frac{1}{r}\frac{\partial}{\partial r}\left(r\mu\frac{\partial u}{\partial r}\right) + \rho g_z \quad (2)$$

Radial component;

$$\rho v\frac{\partial u}{\partial r} + \rho u\frac{\partial u}{\partial Z} = -\frac{\partial p}{\partial r} + \frac{\partial}{\partial Z}\left(r\mu\frac{\partial u}{\partial r}\right) + \frac{2}{r}\frac{\partial}{\partial r}\left(r\mu\frac{\partial u}{\partial r}\right) - \frac{2}{3}\frac{1}{r}\frac{\partial}{\partial r}\left[\mu\frac{\partial}{\partial r}(rv)\right] + \frac{1}{r}\frac{\partial}{\partial r}\left(r\mu\frac{\partial u}{\partial Z}\right) + \frac{\partial}{\partial Z}\left(\mu\frac{\partial u}{\partial r}\right) - \frac{2\mu v}{r^2} + \frac{2}{3}\frac{\mu}{r^2}\left[\frac{\partial u}{\partial r}rv\right] + \frac{2}{3}\frac{\mu}{r}\frac{\partial u}{\partial Z} \quad (3)$$

where μ is the mixture's dynamic viscosity; pressure is denoted by p and gravitational acceleration along the axis denoted by g_z .

Energy equation;

$$c_p\left(\rho v\frac{\partial T}{\partial r} + \rho u\frac{\partial T}{\partial Z}\right) = \frac{1}{r}\frac{\partial}{\partial r}\left(r\lambda\frac{\partial T}{\partial r}\right) + \frac{\partial}{\partial Z}\left(\lambda\frac{\partial T}{\partial Z}\right) - \sum_{K=1}^{KK}\left[\rho c_{p,k}Y_k\left(v_{k,r}\frac{\partial T}{\partial r} + v_{k,Z}\frac{\partial T}{\partial Z}\right)\right] - \sum_{K=1}^{KK}h_k w_k\dot{w}_s - \rho c_{p,s}Y_s\left(v_{Ts,r}\frac{\partial T}{\partial r} + v_{Ts,z}\frac{\partial T}{\partial Z}\right) - h_s w_s\,\dot{w}_s \quad (4)$$

Species conservation equation;

$$\rho v\frac{\partial Y_k}{\partial r} + \rho u\frac{\partial Y_k}{\partial r} = \frac{1}{r}\frac{\partial}{\partial r}(r\rho Y_k u_{k,r}) - \frac{\partial}{\partial Z}(\rho Y_k u_{k,z}) + w_k\dot{w}_k k = 1, \ldots\ldots K \quad (5)$$

where c_P is the mixture specific heat at constant pressure; T is the temperature; the mixture thermal conductivity is denoted λ ; the k[th] heat capacity of the species at constant pressure is denoted by $c_{P,k}$; h_k is the specific enthalpy for the k[th] species; soot specific heat is denoted by $c_{P,s}$; Y_s is the soot mass fraction; $v_{Ts,z}$ and $v_{Ts,r}$ are the soot particles velocities in axial and radial directions respectively; soot specific enthalpy is denoted by h_s; w_s is the soot molecular weight; and $\dot{w}_s$ is the rate of soot production.

Equation of state;

$$p = \rho RT\sum_{k=1}^{KK}\left(Y_k/w_k\right) \quad (6)$$

where Y_k is the k^{th} mass fraction of the species, and the k^{th} axial and radial species velocities are denoted by $v_{k,z}$ and $v_{k,r}$ respectively; w_k represents the k^{th} molecular weight of the species. The total number of gaseous species is KK, and $\dot{w}_k$ is the k[th] molar production rate of the species per unit volume.

2.2. Soot Model

Moss-Brooke's soot model was used for modelling soot formation. The model was used to compute nucleation, surface growth, oxidation rates and soot volume fraction on MLe (C18:3), MLi (C18:2), MO (C18:1), MS (C18:0) and MP (C16:0) flames. This model was used due to its compatibility with non-premixed combustion model [20]. Acetylene (C_2H_2) radicals were considered as major soot precursors during the modeling. The mass and nuclei concentration in this model were obtained using Eq. (7) and (8) respectively [21].

$$\frac{\partial}{\partial t}\rho Y_{soot} + \Delta\cdot(\rho v Y_{soot}) = \Delta\cdot\left(\frac{\mu_t}{\sigma_{soot}}\Delta Y_{soot}\right) + \frac{dM}{dt} \quad (7)$$

$$\frac{\partial}{\partial t}\rho b^*_{nuc} + \Delta\cdot(\rho v b^*_{nuc}) = \Delta\cdot\left(\frac{\mu_t}{\sigma_{nuc}}\Delta Y_{nuc}\right) + \frac{1}{N_{norm}}\frac{dN}{dt} \quad (8)$$

where ρ is the soot density, Y_{soot} is mass fraction of soot , σ_{soot} is the soot prandtl number, σ_{nuc} is the nuclei transport prandtl number, m is mass concentration of soot (kg/m^3), μ_t denotes the dynamic viscosity coefficient, b^*_{nuc} is the concentration of nuclei (particles $\times 10^{-15}$/kg) = $\frac{N}{\rho Nnorm}$, v is the mass stoichiometry and N is the number density for a soot particle (particles/m^3) N_{norm} = 1015 particles. The immediate rate of soot production which depends on coagulation and gas phase nucleation is given by Eq. (9).

$$\frac{dN}{dt} = \left[C_\alpha N_A \left(\frac{X_{prec}\, P}{RT}\right)^{l} exp\left(-\frac{T_\alpha}{T}\right)\right] - \left[C_\beta \left(\frac{24RT}{\rho_{soot}}\right)^{\frac{1}{2}} d_p^{\frac{1}{2}} N^2\right] \quad (9)$$

The model constants are $C_{\beta,}$ C_α and l. N_A is Avogadro number (N_A = 6.022045x10 ^{26} kmol $^{-1}$), X_{prec} is the precursor mole fraction, T_α is the soot inception, P is the pressure, R is the molar constant and d_p is the soot diameter. Soot density was considered as 1800 kg/m^3 [7]. Luque *et al* [22] reported that acetylene (C_2H_2), ethylene (C_2H_4) and propylene (C_3H_6) were major intermediate species during combustion of palm oil methyl esters while C_2H_2 was found on both rich and lean sides of the flame, therefore making it suitable to be considered as the soot precursor in this study. Soot mass concentration was modelled using Eq. (10).

$$\frac{dM}{dt} = \left[C_\alpha M_p \left(\frac{X_{prec}\, P}{RT}\right)^{l} exp\left(-\frac{T_\alpha}{T}\right)\right] + \left[C_\gamma \left(\frac{X_{sgs}\, P}{RT}\right)^{m} exp\left(\frac{T_\gamma}{T}\right)\left(\pi N^{\frac{1}{3}}\right)\frac{6M}{\rho_{soot}}^{\frac{2}{3n}}\right] - \left[C_{oxide} C_w n_{coll} \left(\frac{X_{OH}\, P}{RT}\right)\sqrt{T}\pi N^{\frac{1}{3}}\left(\frac{6M}{\rho_{soot}}\right)^{\frac{2}{3}}\right] \quad (10)$$

where M and N are additional model constants. The constant M_P (144 kg/kgmol) is the mass of an incipient soot particle considered for 12 carbon atoms, where the model constants C_ω, C_γ and C_{oxid} are also included. T_Y is the surface growth activation temperature, X_{OH} is the hydroxyl radical mass concentration and X_{sgs} are participating species in mole that are responsible for surface growth.

2.3. Boundary Conditions

The schematic diagram of the flow configuration is shown in Fig. 1. It is a 2-D axisymmetric co-flow configuration with the dimensions shown in Fig. 1. The domain was set to be large enough to ensure that the flame is fully developed through eliminating the effect of the boundary conditions [23].

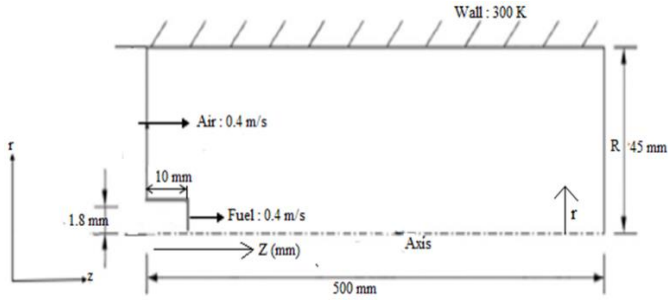

Fig. 1. Schematic diagram of computational domain.

The model dimensions in Fig. 1 were achieved through several simulations of fuel combustion at different domain dimension. The temperatures were noted and graph plotted to show the changes in combustion temperatures. Negligible temperatures changes were noted at width of 40 mm and 45 mm and the height of 400 mm and 500 mm as shown in Fig. 4. Therefore, the length of 500 mm and width of 45 mm were selected since the flame was fully developed and it recorded minimal change in temperature.

A uniform inlet velocity profile of both air and fuel stream are adopted. The inlet mass fraction of N_2 and O_2 are set at 0.233 and 0.767 in co-flow air, respectively. The velocity and temperature at the inlet were set at 0.4 m/s and 300 K respectively. The velocity of 0.4 m/s was used since it is in the range of laminar burning velocity of biofuel [24]. The model temperature and pressure were set at normal room conditions while gauge pressure at the outlet was set at zero. Stationary burner walls with no-slip conditions and convective heat transfer were adopted.

ANSYS Fluent package which is inbuilt in ANSYS work bench software (version 2022 R1) was used to solve the equations of a steady state combustion for non-premixed, laminar co-flow diffusion flame. The energy, momentum, continuity, and species equations were all solved using the pressure-based solver. The chemical reaction are based on the FAME mechanism from CRECK modeling group, which has 2904 chemical reactions and 177 species [25]. The mechanism was selected due to its ability to show the physio-chemical properties and chemical structure of major esters of biodiesel fuel. Experimental datasets from key FAME components have been used to validate this model [26].

2.4 Mesh refinement

The computational domain was discretized into a mesh of rectangular elements. The mesh was progressively refined to a level where results were grid independent. To this end, a level of 373,280 was sufficient. A section of mesh distribution at the inlet of the domain adopted is shown in

Fig. 2. The tests and the results given in Fig. 3, served as the basis for the mesh size selection. Mesh sizes of 373,280, 320,000, 93,944, and 46,977 elements were used in the mesh test. The mesh refinement was uniformly done along *Z* and *r* axis.

Fig. 2. Section of mesh distribution at the inlet.

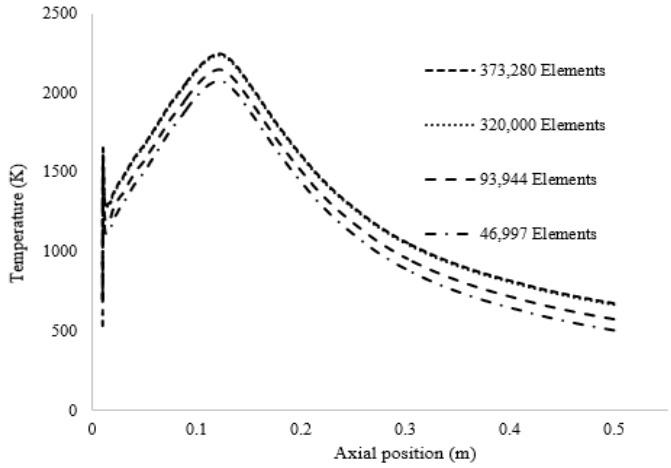

Fig. 3. Comparison of temperature profile along the axis for MLe when using various mesh sizes.

2.5 Model validation

The main limitation of this study was lack of experimental data on combustion of individual biodiesel methyl esters. Though there is no experimental data, the model flame temperatures were validated using biodiesel methyl esters temperature range because methyl esters investigated in this study are the major biodiesel components. The computed temperature range in this study is in good agreement with those of Jeon *et al.* [27] and Mao *et al.* [28], which reported temperature range between 2000 K and 2500 K for biodiesel combustion. Therefore, this model can be used to investigate how major components of biodiesel affect the amount of soot produced in biodiesel co-flow flames.

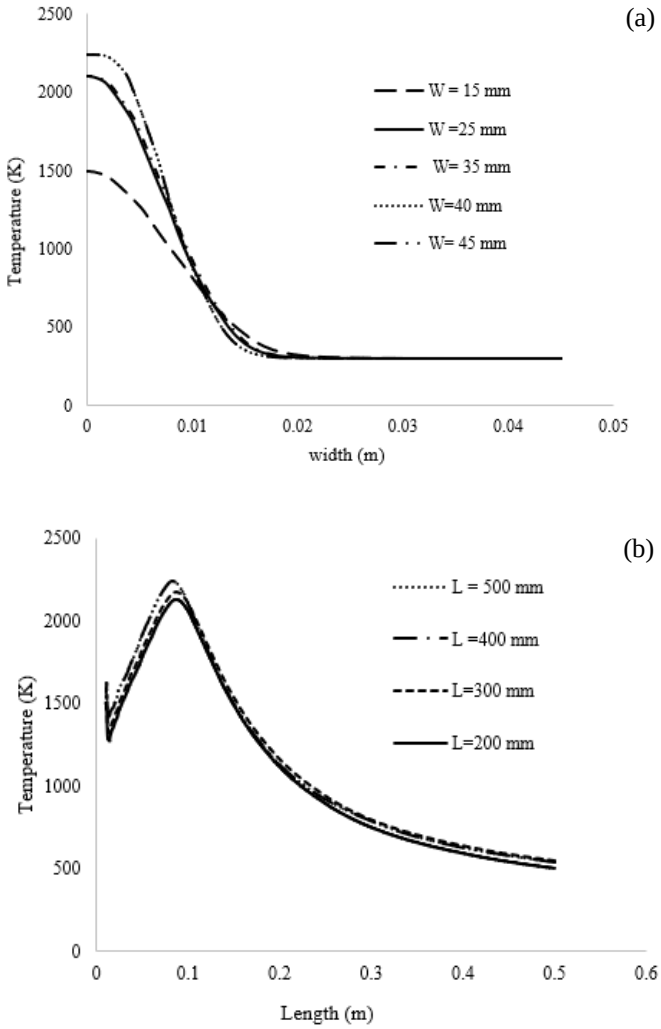

Fig. 4. Computed temperature profiles for (a) width validation, (b) length validation.

3. Results and Discussion

Radial flame temperature profiles at different positions of Z axis for the five methyl esters are presented in Fig. 4. The graphs reveal that the flame temperatures in all methyl esters exhibit the same profile. The flame temperatures in all methyl esters are higher at the center except for the lower region below an axial distance of 50 mm from the inlet. The lift off occurs at the lower region close to the burner hence causing lower temperatures. Higher temperature at the center of the flame is due to the ideal air/fuel ratio which aids in complete combustion thus producing the highest heat density at the region [27]. According to the profiles, Fig. 5(a)-(e), the highest flame temperatures occurred at 80 mm measured in the radial direction from the axis. This indicates a region where there is optimum combustion due to proper mixing of air and fuel. At any corresponding axial distance, flame

temperatures are highest in MLe as compared to other methyl esters, as shown in Fig. 5(a). At any corresponding axial distance, flame temperatures are highest in MLe as compared to other methyl esters, as shown in Fig. 5(a)-(e). For example, at Z = 50 mm MLe, MLi, MO, MS and MP recorded a maximum temperature of 2170 K, 2145 K, 2122 K, 2100 K and 2091 K respectively. On the other hand, MS had the lowest flame temperature, as seen in Fig. 5(d). All methyl esters investigated showed a decrease in temperature at radial distance above 0.01 m. The temperatures decrease and then slowly falls to room temperatures in all flames. In all flames, an increment in axial distance Z resulted in temperature falling slowly to room temperatures at different radial position as shown in fig. 5(a)-(e). This portrays the different flame width at different axial distances.

Generally, the flame temperatures are higher in unsaturated methyl esters compared to saturated methyl esters. Temperature increases as the number of carbon double bonds increased in unsaturated methyl esters because more energy is required to break the double bonds. Although both MP and MS are completely saturated, the temperature for MP was slightly higher than that for MS. This difference can be attributed to the fact that MP has a shorter carbon chain, which necessitates more energy to be broken compared to MS.

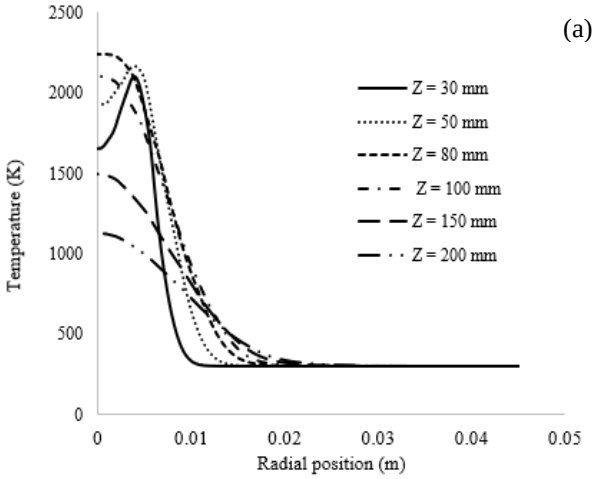

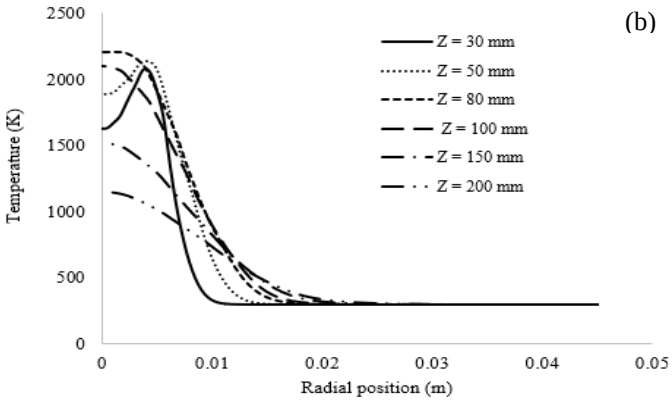

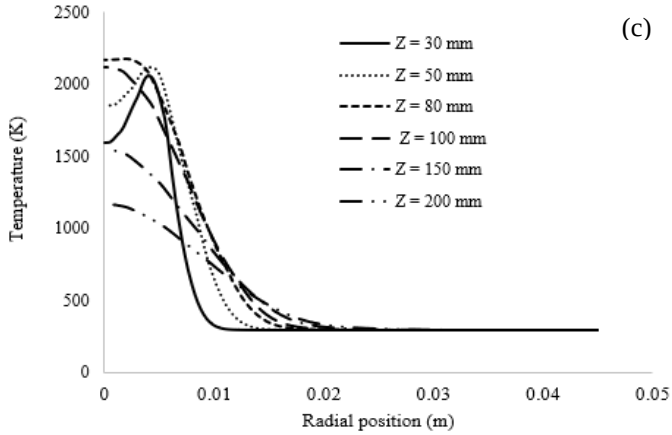

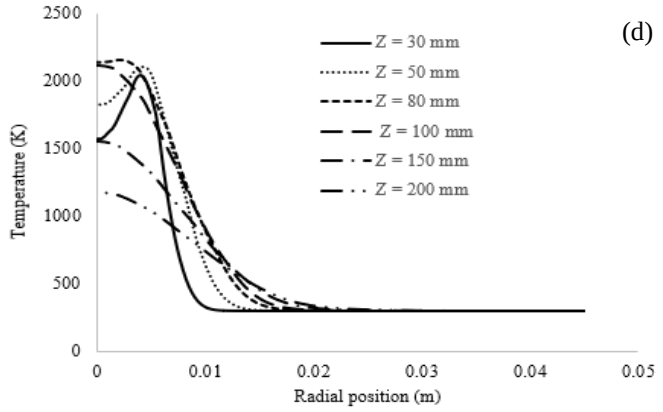

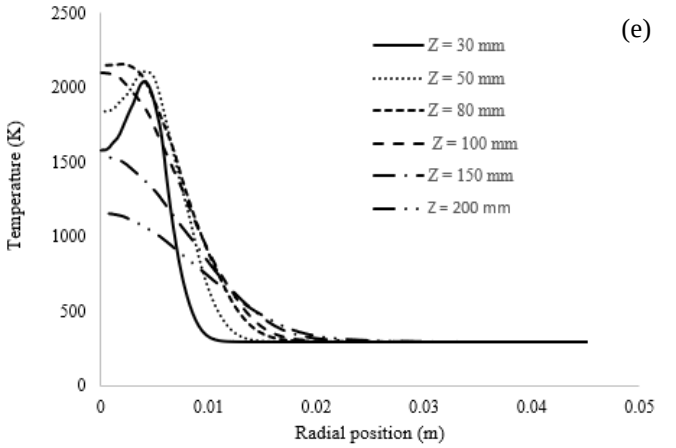

Fig. 5. Computed temperature profiles along the radius for (a) MLe, (b) MLi, (c) MO, (d) MS and (e) MP.

Soot nucleation is essentially transition from molecular precursors in the gas phase to condensed particulate matter phase [29]. In Moss-Brooke's soot model, acetylene (C_2H_2) is considered a major soot precursor during the computation of nucleation rate. Nucleation rates contour for various methyl esters are presented in Fig. 6 while nucleation rates along the radius at different axial positions are presented in Fig. 7. In all methyl esters, the rates are higher at the centerline of flames for the regions above 70 mm axially from the inlet. The rates decrease along the flame wings due to the drop in combustion temperature as shown in Fig. 7(a)-(e). The region with higher nucleation rates for the lower part (below 70 mm axially) are shifted towards the outer part of radius. Combustion region with high nucleation rates correspond to areas of higher temperatures observed in Fig. 5. This indicates that temperatures have direct impact on soot nucleation rates. MLe exhibited the highest nucleation rates while MS had the lowest. Soot nucleation rates are lower in saturated methyl esters and increases as the ester becomes unsaturated. The higher nucleation rate in MLe as compared to other methyl esters can be attributed to its higher aromatic content which enhances nucleation rate. During pyrolysis, C_2H_2 and other major intermediate species are produced which act as soot precursors. MLe produced the highest mole fraction of acetylene and benzene compared to other major methyl esters. As the level of unsaturation increases, the production of acetylene and benzene increases as shown in Fig. 8 and Fig. 9. Similar observation was established by Wang *et al.* [30] in their study of soot formation in biodiesel combustion in diesel engines. Similarly, Matti *et al.* [31] reported an increase in rate of soot formation when benzene was added to the fuel due to enhanced production of aromatics and PAHs. Higher aromatic content in fuel results in earlier soot inception and increased soot emissions [12].

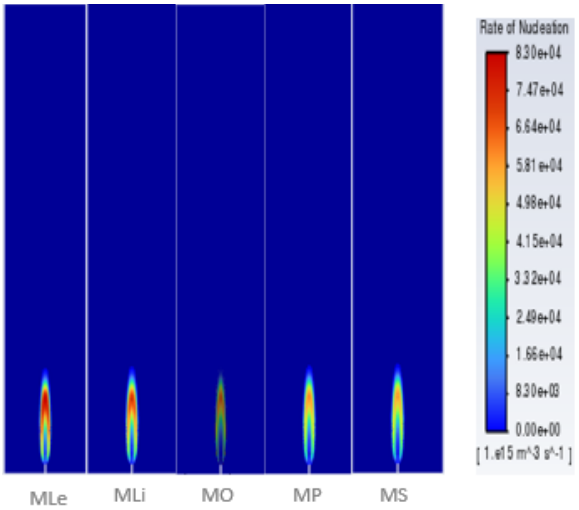

Fig. 6. Contours of nucleation rates for MLe, MLi, MO, MP and MS.

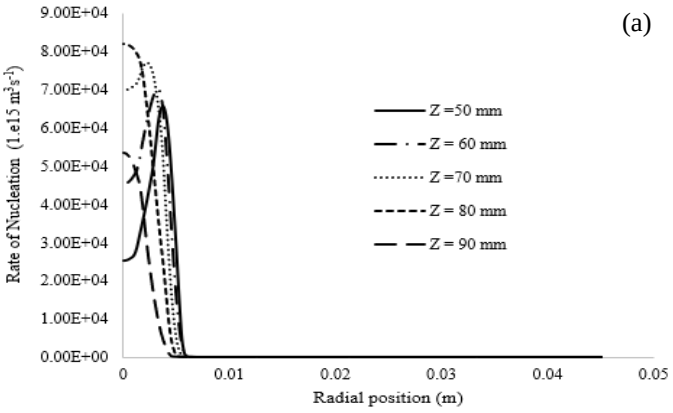

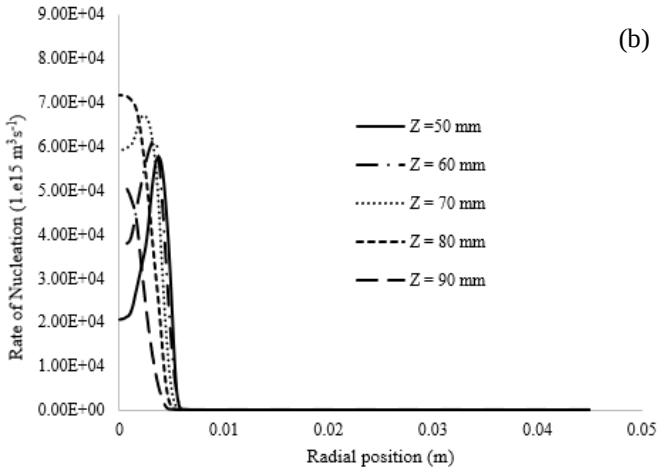

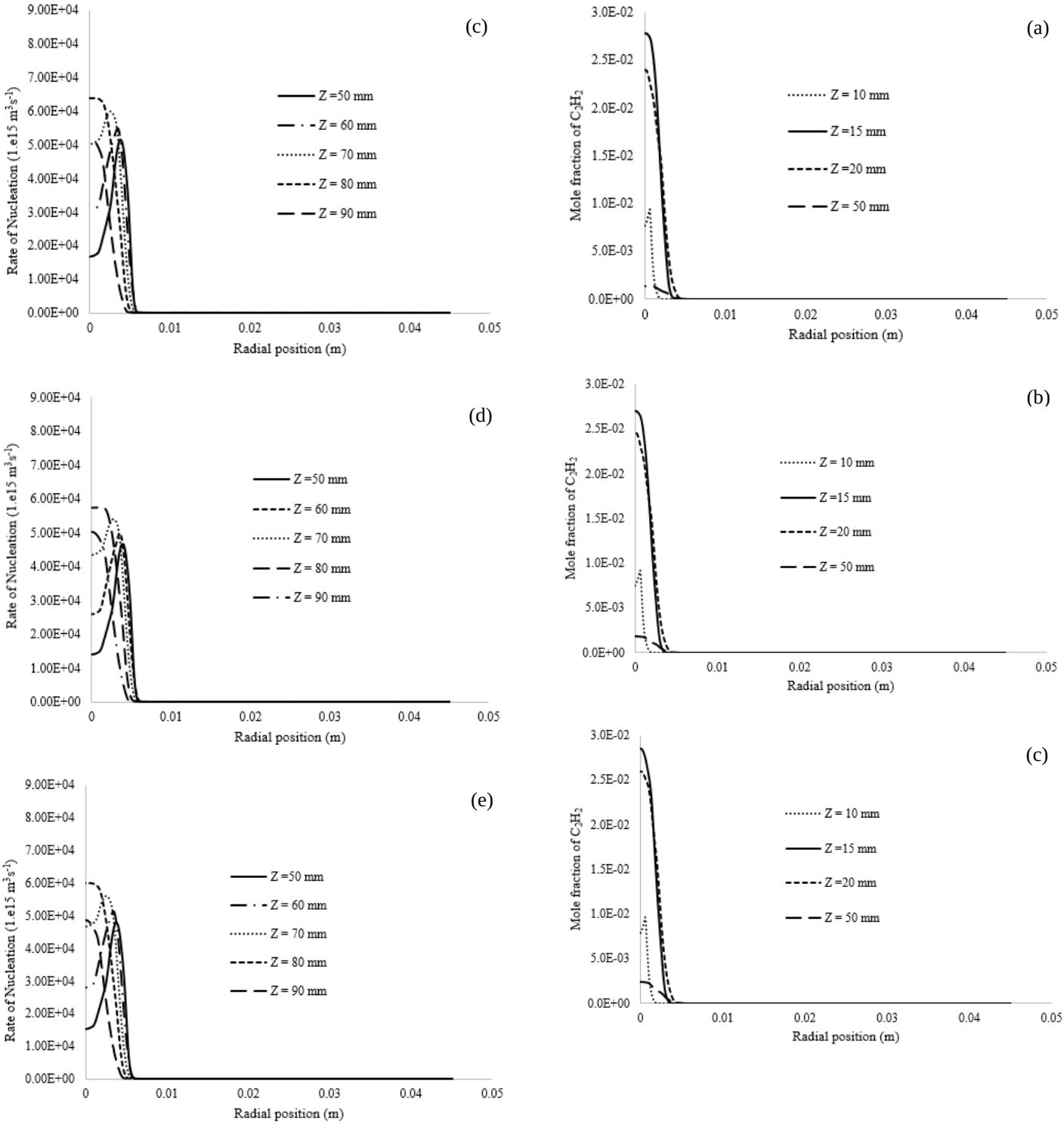

Fig. 7. Computed nucleation rates along the radius for (a) MLe, (b) MLi, (c) MO, (d) MS and (e) MP.

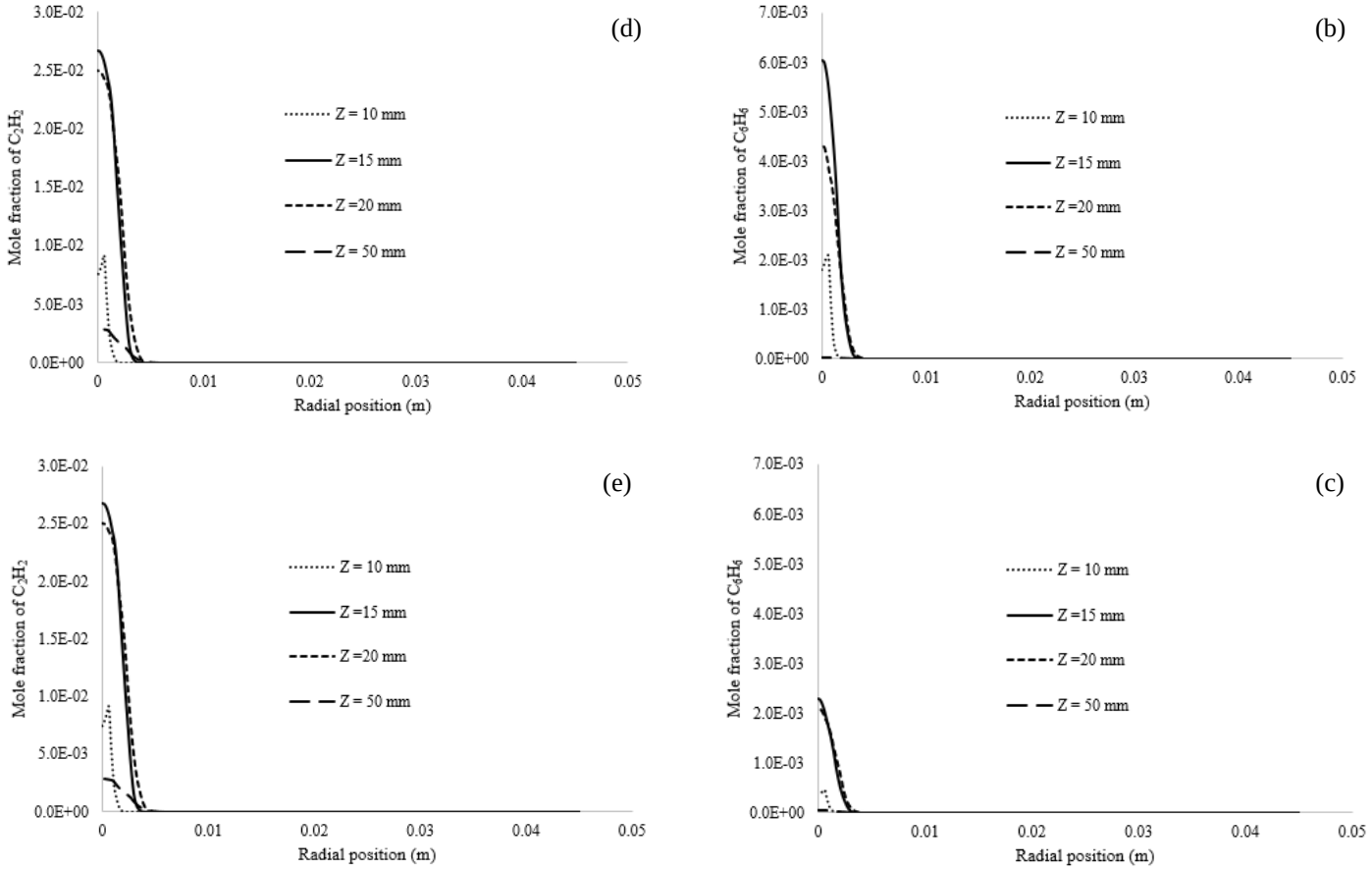

Fig. 8. Computed mole fraction of C_2H_2 along the radius for (a) MLe, (b) MLi, (c) MO, (d) MS and (e) MP.

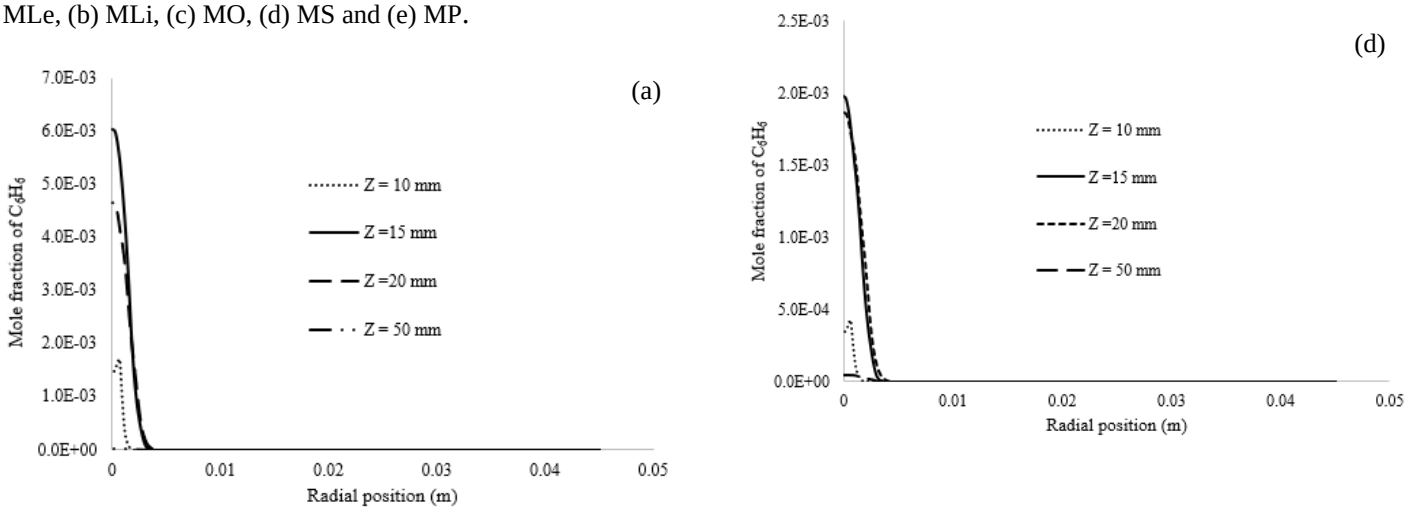

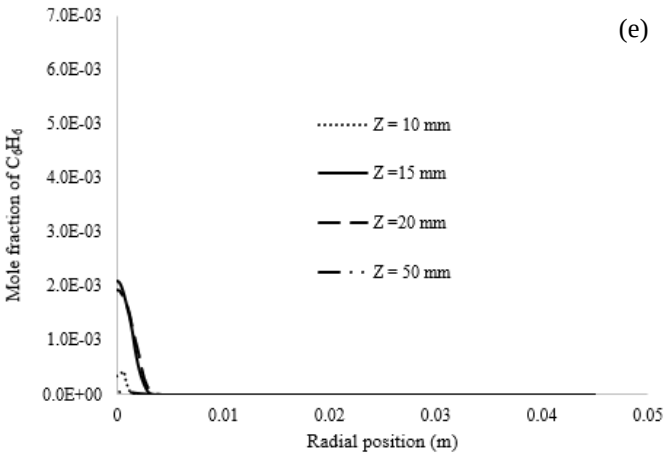

Fig. 9. Computed mole fraction of C_6H_6 along the radius for (a) MLe, (b) MLi, (c) MO, (d) MS and (e) MP.

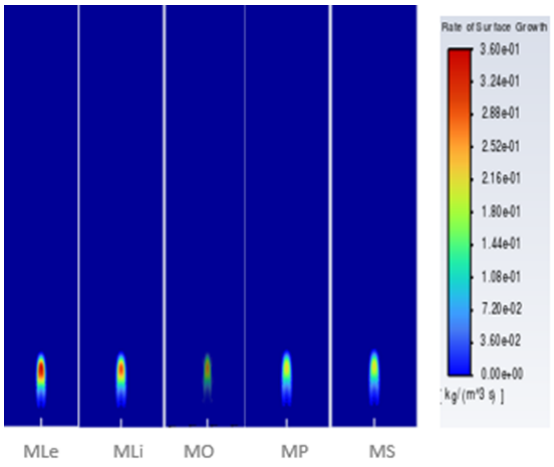

Fig. 10. Surface growth rate contours in major methyl esters.

Surface growth is the reaction of soot surface and gas which arises simultaneously with coagulation [32]. Reaction between acetylene and soot particle's surface in this process results in increase in volume of soot particle. Higher surface growth rates were observed at the centerline of all flames which decreases along the flame wings as shown in Fig. 10 and Fig. 11. MLe presented a higher surface growth rate while the lowest surface growth rates were observed in MS flames. Surface growth rates at Z = 50 mm increase slowly from the center then decreases across the wings in all flames. This is attributed to inception of surface growth rates in all flames. MLe presented a higher surface growth rate while the lowest surface growth rates were observed in MS flames. Higher rate of surface growth in MLe flame is as a result of relatively higher portions of surface sites available for the reaction. It is also due to higher aromatic content and higher flame temperature. The results show that the surface growth rates increase with the increase in level of unsaturation and high aromatic content. Similarly, a study conducted by Tian *et al.* [7] on biodiesels and methyl esters diffusion flames established that, aromatic content was a key contributor to soot inception and higher growth rate.

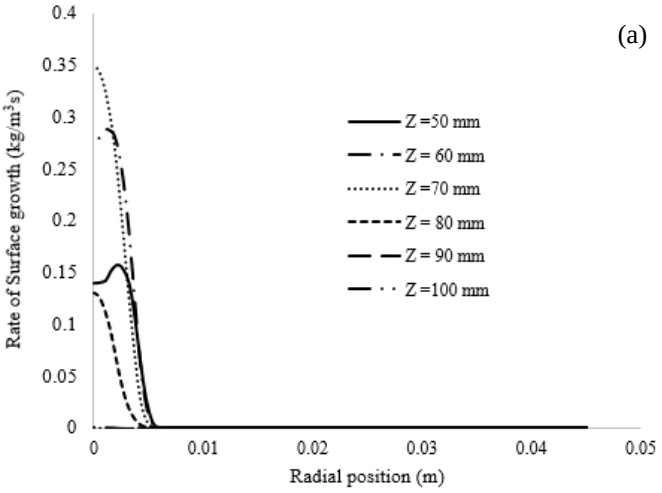

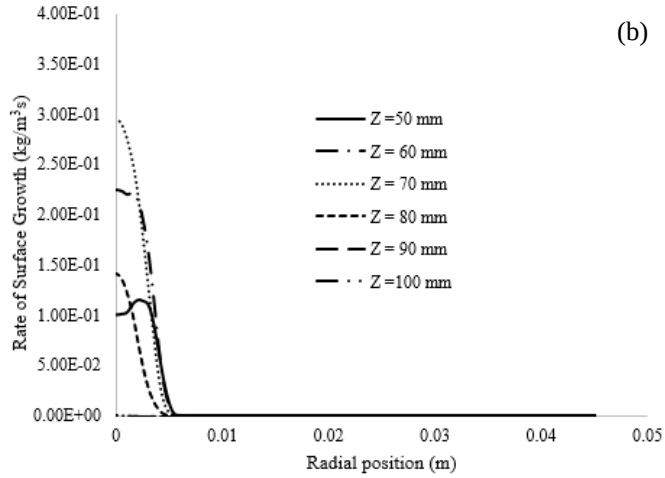

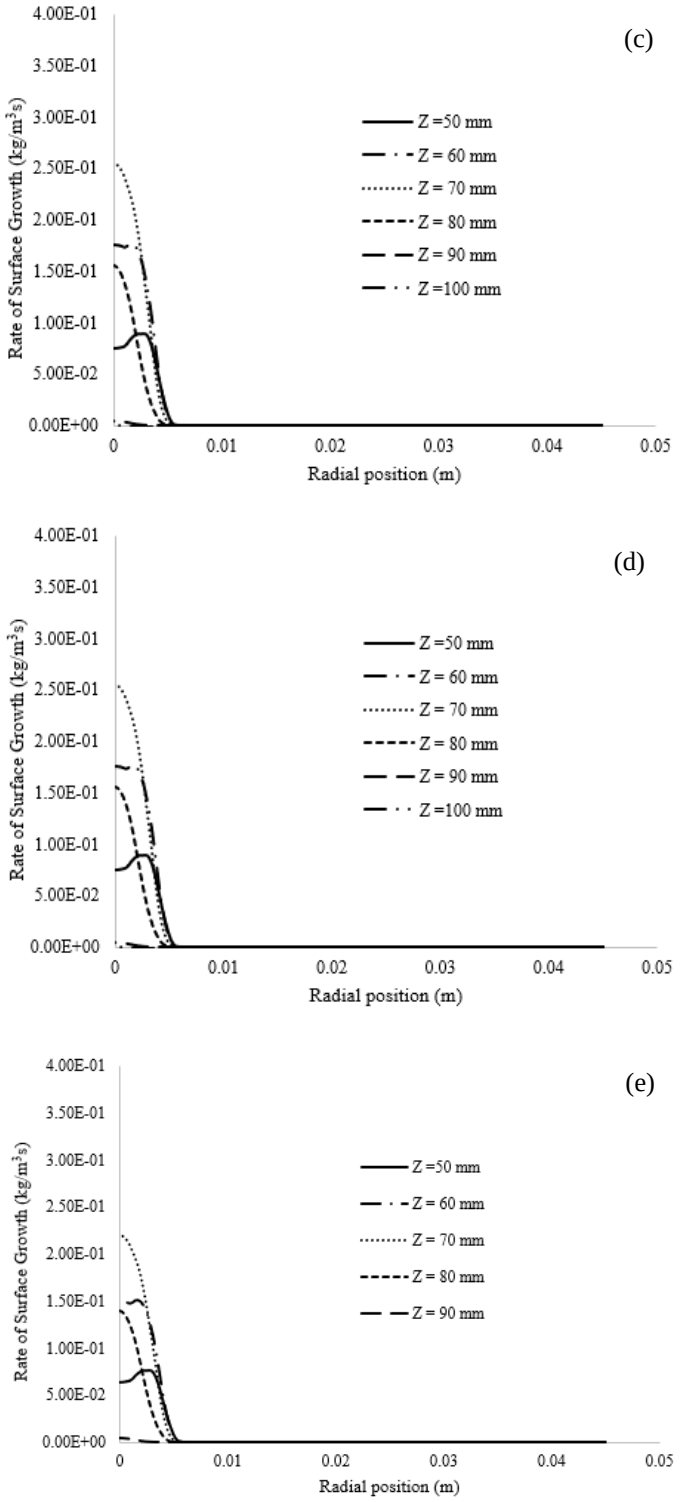

Fig. 11. Computed surface growth rates along the radius for (a) MLe, (b) MLi, (c) MO, (d) MS and (e) MP.

Coagulation occurs when two primary soot particles collide resulting in an increase in soot particle size. It is assumed that a larger spherical particle is formed when the two particles fully merge preserving total soot volume [31]. According to experimental results by Wang *et al.* [33], the density of primary particle of soot is almost constant over the growing area of the flame. Coagulation rates along the radius at different axial positions for various methyl esters are presented in Fig. 12 while contours of coagulation rates are shown in Fig. 13. The graphs show that higher coagulation rates occur at the centerline of all flames for the flame region above 70 mm axially from the inlet. Lower combustion region below 70 mm from the inlet has higher coagulation rates occurring towards the outer parts of the radius as seen in Fig. 11(a)-(e). In general, unsaturated methyl esters have higher coagulation rates while saturated esters have low coagulation rates. MLe displayed the highest coagulation rates while MS presented the lowest coagulation rates as shown in Fig. 12 and Fig. 13. The rise in coagulation rate with respect to temperature is due to higher collision of soot particles after surface growth due to increased combustion temperatures. Coagulation rates reduced as the combustion temperature reduced. A higher rate of coagulation was observed in MLe flame due to high flame temperature which causes high collision of soot particles.

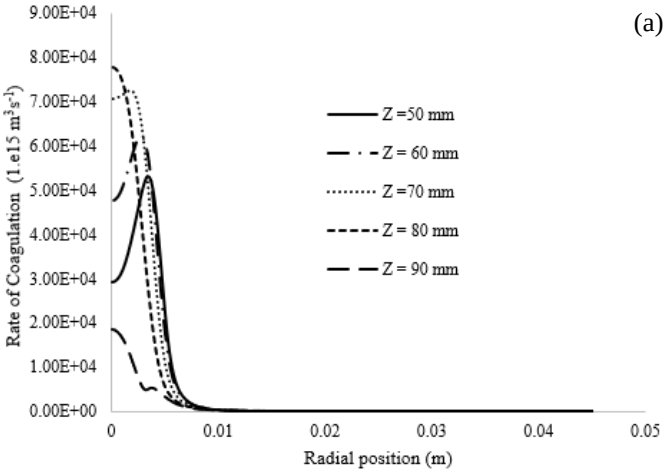

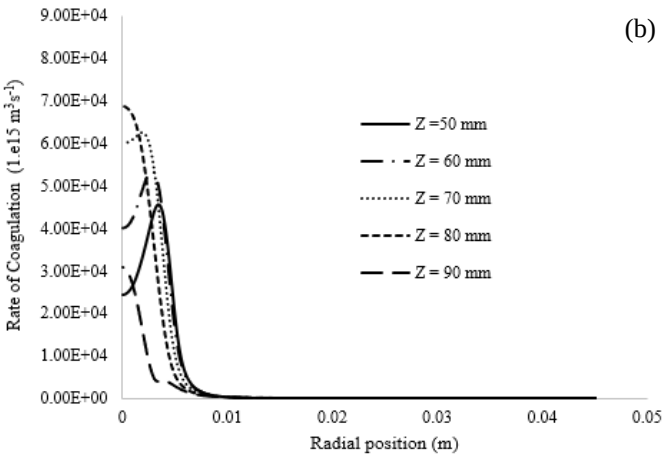

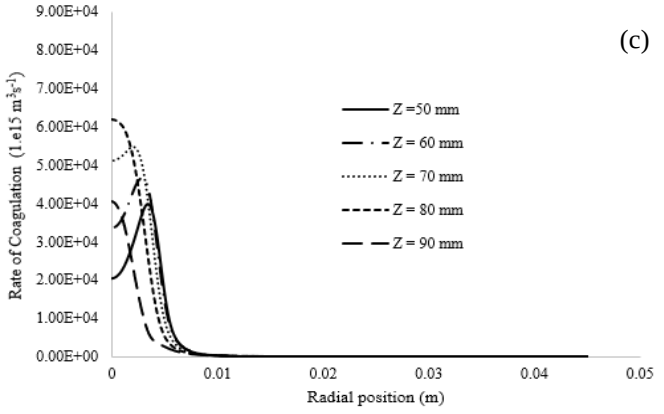

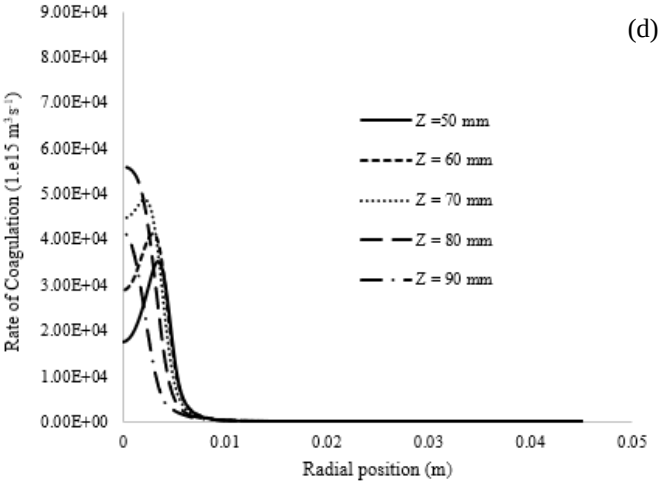

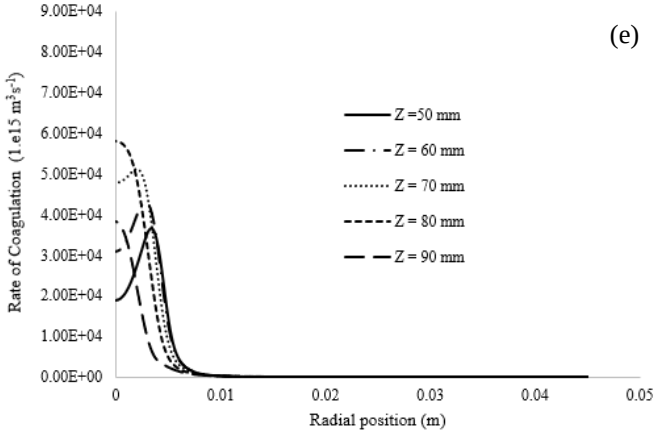

Fig. 12. Computed coagulation rates along the radius for (a) MLe, (b) MLi, (c) MO, (d) MS and (e) MP.

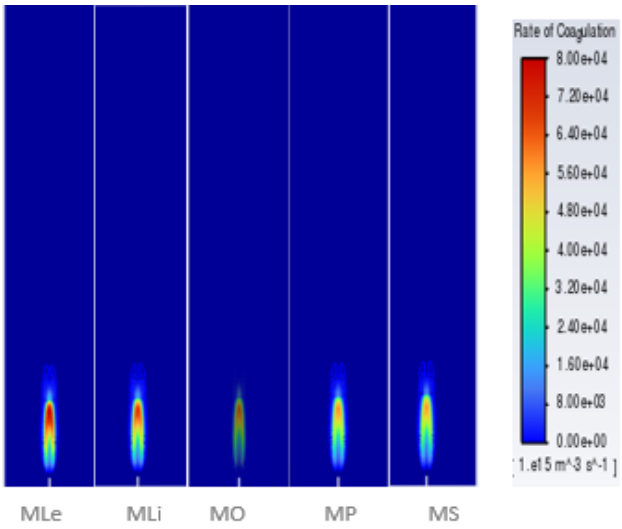

Fig. 13. Coagulation rate contours in biodiesel major methyl esters.

Soot particle size is reduced by oxidation reaction. Oxidation occurs on the surface area of soot particles whenever in contact with the oxidant species. Oxygen and hydroxyl radical are the dominant oxidant species [34]. Contours of oxidation rate for various methyl esters are presented in Fig. 14 while oxidation rate along the radius at different axial position is shown in Fig. 15. In the upper part of the flame (above 80 mm), all methyl esters show a high oxidation rate at the centerline which reduces along the radius. On the other hand, high oxidation rates occur away from the axis for lower flame region in all methyl esters as seen in Fig. 15(a)-(e). The oxidation rates increased with increased level of unsaturation which shows low oxidation in saturated MS and high oxidation in unsaturated MLe. High oxidation rate by MLe is as a result of increased oxidant species and flame temperatures. Unsaturated methyl esters have higher

flame temperature, which may be responsible for higher rates of soot oxidation. According to numerical research on the combustion of polycyclic aromatic hydrocarbons, high temperatures results in higher soot oxidation [35].

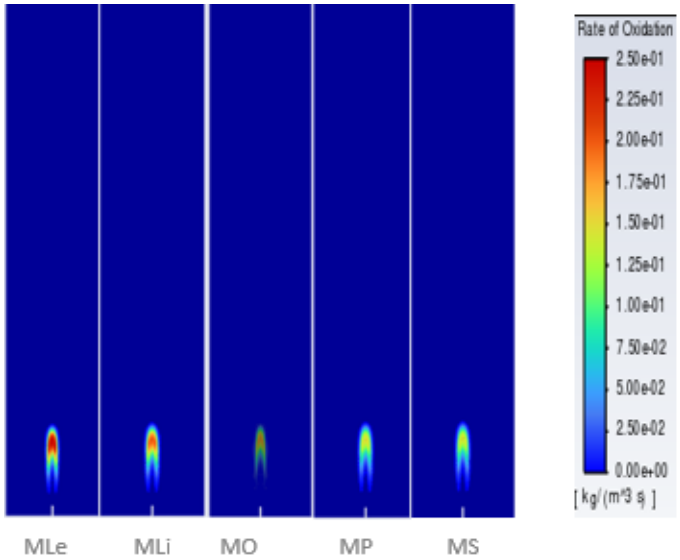

Fig. 14. Rate of oxidation contours for major methyl esters.

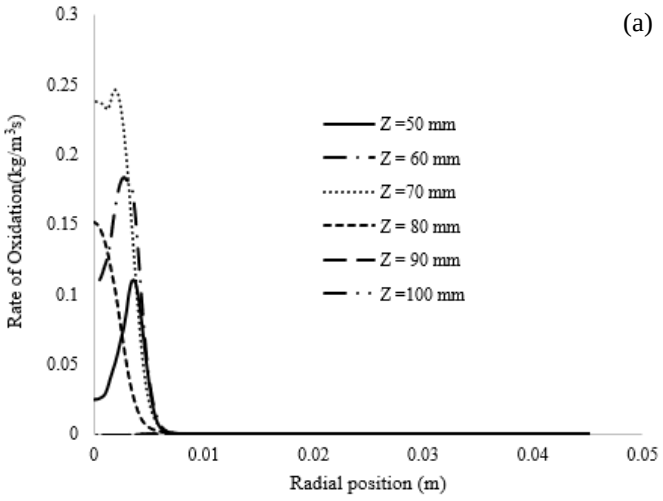

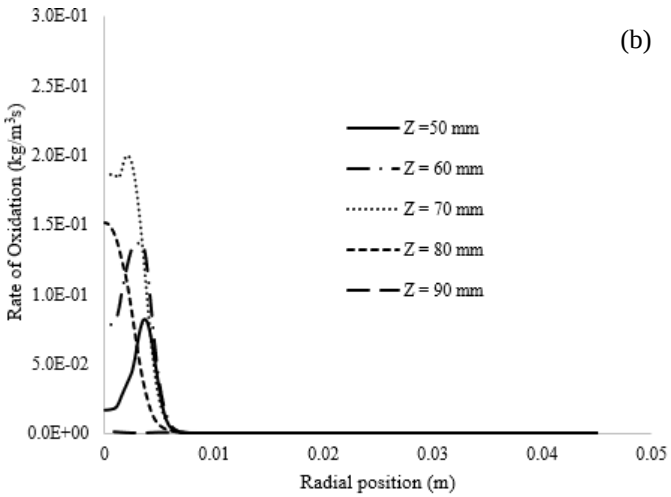

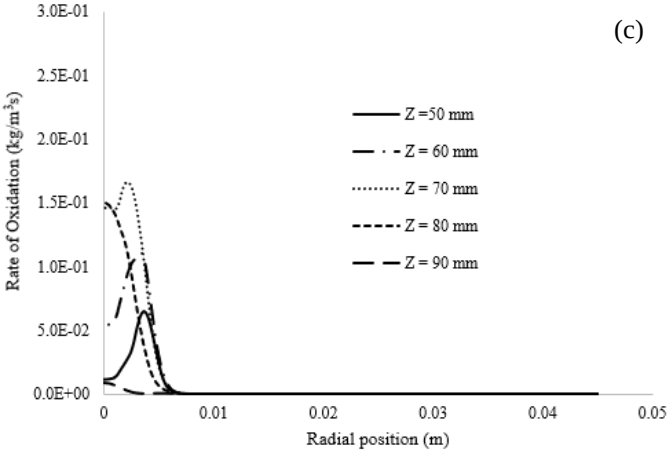

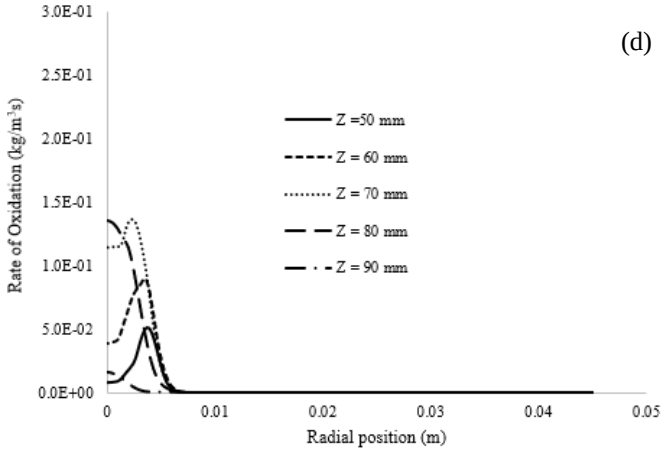

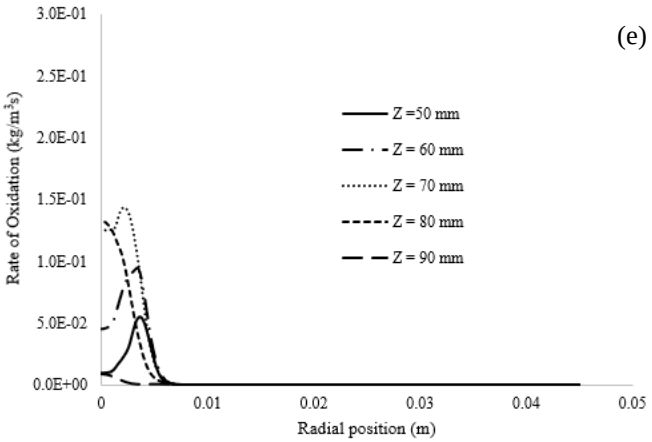

Fig. 15. Computed Oxidation rates along the radius for (a) MLe, (b) MLi, (c) MO, (d) MS and (e) MP.

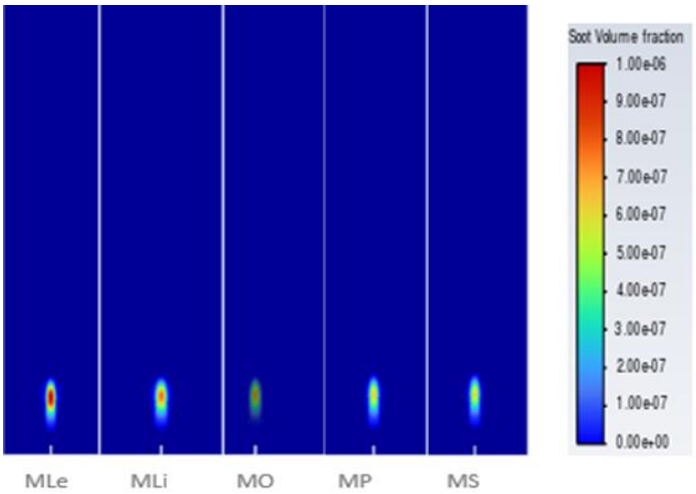

Fig. 16. Soot volume fraction contours.

The knowledge on soot production mechanisms and soot distribution are key issues in many aspects of combustion [36]. Contours of soot volume fraction for various methyl esters are presented in Fig. 16 while soot volume fraction along the radius at different axial positions are presented in Fig. 17. It was observed that all methyl esters showed the highest soot volume at the axis which then reduces from it. In all the flames, Fig. 17(a)-(e), the highest soot volume fraction shifts from the flame's wings to the centerline. Shifting of maximum soot fraction is attributed to a reduction in soot zone residence time, which is attributed to less time for surface growth to produce soot along the flame wings [37]. Soot volume fraction rose with increased level of unsaturation which showed low soot volume in saturated MS and high soot volume in unsaturated MLe. Higher soot volume fraction in MLe flame as compared to other methyl esters is due to a higher aromatic content in the fuel. Studies conducted on the influence of fuel aromaticity on soot volume fraction showed that a higher aromatic fuel has a higher growth rate and higher soot volume fraction [38].

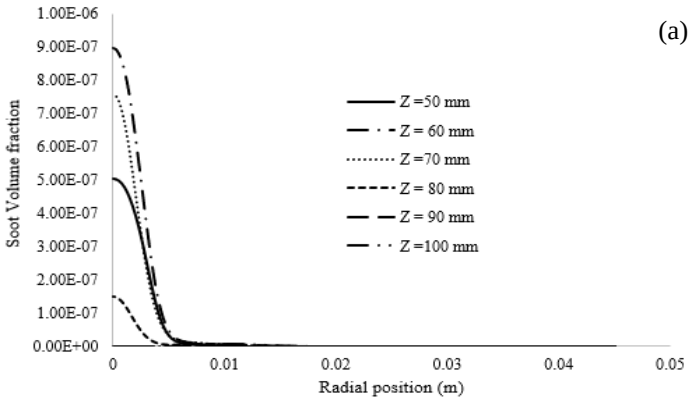

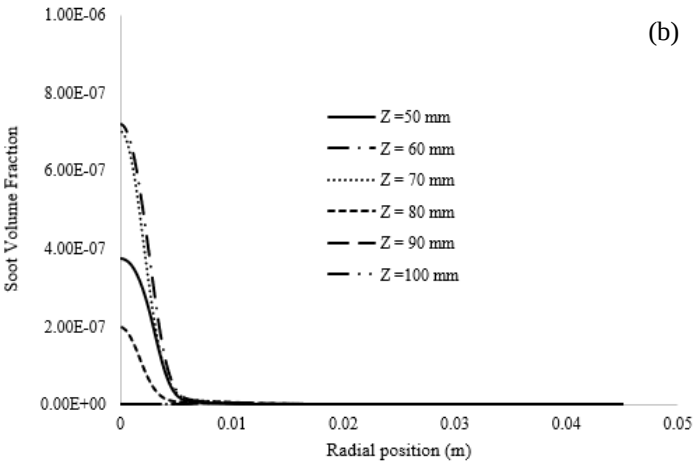

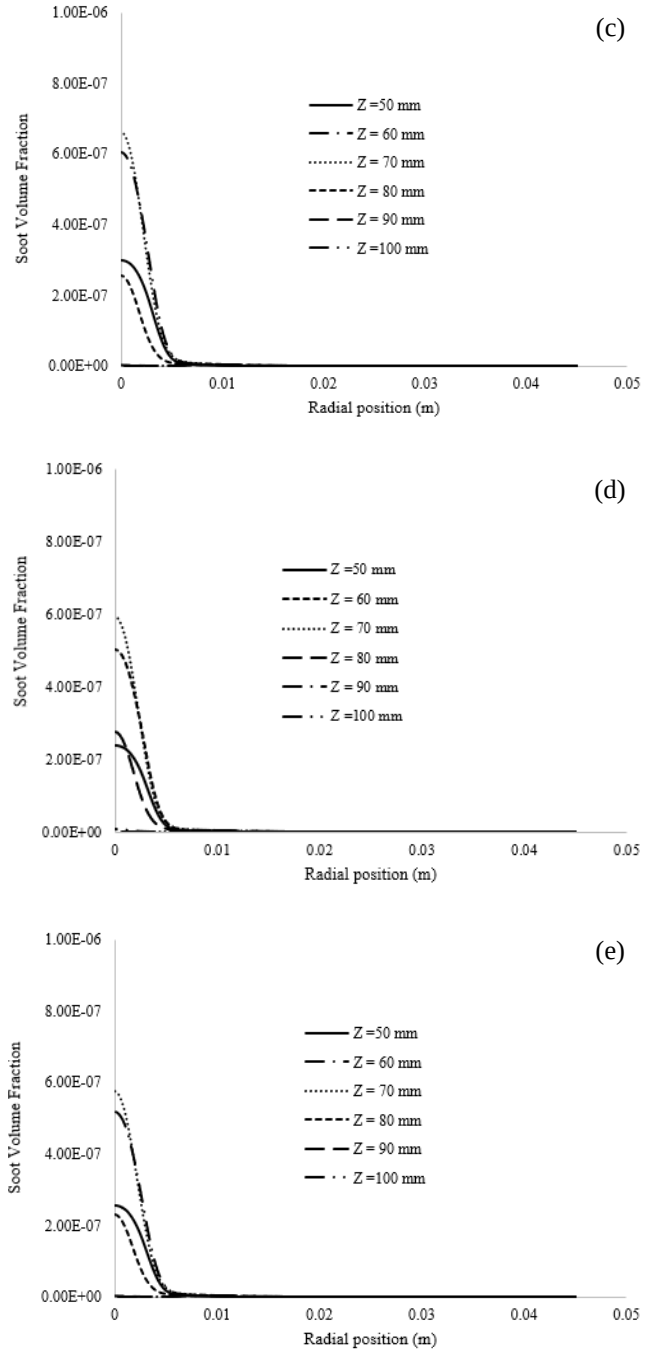

Fig. 17. Computed soot volume fraction along the radius for (a) MLe, (b) MLi, (c) MO, (d) MS and (e) MP.

4. Conclusions

This study focused on the influence of MLe, MLi, MO, MS and MP on soot formation in biodiesel co-flow flame by studying each in isolation and mapping out the nucleation rates, coagulation rates, surface growth, oxidation rates and soot volume fraction across the flames. The following are the main findings:

- MLe had the greatest influence in soot formation while MS has the least. The MLe generates the highest concentration of aromatic compounds and is linked to the higher number of carbon double bonds. In this environment of low concentration of hydrogen and hydroxyl radicals the carbon form aromatic radicals. Aromatic radicals are critical precursors for soot formation.
- Nucleation rates, coagulation rates, surface growth rates, oxidation rates and soot volume fraction increase with increase in carbon double bonds.
- Biodiesels with shorter carbon chain of saturated methyl esters have high propensity to form soot as compared to biodiesel with longer carbon chains components.

Therefore, biodiesels that have high composition of methyl esters with high number of carbon double bonds have higher propensity to form soot as compared to those with few numbers or no carbon double bond.

Acknowledgement

This study was funded by Dedan Kimathi University of Technology, Kenya.

References

[1] R. M. El-Zoheiry, A. I. EL-Seesy, A. M. A. Attia, Z. He, and H. M. El-Batsh, "Combustion and emission characteristics of Jojoba biodiesel-jet A1 mixtures applying a lean premixed pre-vaporized combustion techniques: An experimental investigation," *Renew. Energy*, vol. 162, pp. 2227–2245, 2020, doi: 10.1016/j.renene.2020.10.031.

[2] A. A. Shankar, P. R. Pentapati, and R. K. Prasad, "Biodiesel synthesis from cottonseed oil using homogeneous alkali catalyst and using heterogeneous multi walled carbon nanotubes : Characterization and blending studies," *Egypt. J. Pet.*, vol. 26, no. 1, pp. 125–133, 2017, doi: 10.1016/j.ejpe.2016.04.001.

[3] B. Jiang, D. Liu, and Z. Lin, "Soot particles diagnostics in ethylene inverse diffusion flame blending with biodiesel surrogates of saturated methyl butyrate and unsaturated methyl crotonate," *Fuel Process. Technol.*, vol. 202, p. 106379, 2020, doi: 10.1016/j.fuproc.2020.106379.

[4] M. S. Celnik, M. Sander, A. Raj, R. H. West, and M. Kraft, "Modelling soot formation in a premixed flame using an aromatic-site soot model and an improved oxidation rate," *Proc. Combust. Inst.*, vol. 32 I, no. 1, pp. 639–646, 2009, doi: 10.1016/j.proci.2008.06.062.

[5] D. O. Lignell, J. H. Chen, P. J. Smith, T. Lu, and C. K. Law, "The effect of flame structure on soot formation and transport in turbulent nonpremixed flames using direct numerical simulation," *Combust. Flame*, vol. 151, no. 1–2, pp. 2–28, 2007, doi: 10.1016/j.combustflame.2007.05.013.

[6] H. Wang, H. Wang, and L. P. Flames, "Combustion Chemistry," *Oil Gas Sci. Technol.*, 2015, [Online]. Available: doi: 10.2516/ogst/2016011.

[7] B. Tian *et al.*, "Experimental and numerical study on soot formation in laminar diffusion flames of biodiesels and methyl esters," *Proc. Combust, Inst*, vol. 38, pp. 1335–1344, 2020, doi: 10.1016/j.proci.2020.06.074.

[8] A. D. Anna and M. Sirignano, "Detailed kinetic mechanisms of PAH and soot formation 12," vol. 45, 2019, doi: 10.1016/B978-0-444-64087-1.00012-7.

[9] A. Khosousi and S. B. Dworkin, "Soot surface reactivity during surface growth and oxidation in laminar diffusion flames," *Combust. Flame*, vol. 162, no. 12, pp. 4523–4532, 2015, doi: 10.1016/j.combustflame.2015.09.005.

[10] Z. Gao, L. Zhu, X. Zou, C. Liu, B. Tian, and Z. Huang, "Soot reduction effects of dibutyl ether (DBE) addition to a biodiesel surrogate in laminar coflow diffusion flames," *Proc. Combust. Inst.*, vol. 37, no. 1, pp. 1265–1272, 2019, doi: 10.1016/j.proci.2018.05.083.

[11] C. T. Chong and S. Hochgreb, "Spray flame structure of rapeseed biodiesel and Jet-A1 fuel," *Fuel*, vol. 115, pp. 551–558, 2014, doi: 10.1016/j.fuel.2013.07.059.

[12] J. Reijnders, M. Boot, and P. De Goey, "Impact of aromaticity and cetane number on the soot-NOx trade-off in conventional and low temperature combustion," *Fuel*, vol. 186, pp. 24–34, 2016, doi: 10.1016/j.fuel.2016.08.009.

[13] C. T. Chong and S. Hochgreb, "Flame structure, spectroscopy and emissions quantification of rapeseed biodiesel under model gas turbine conditions," *Appl. Energy*, vol. 185, pp. 1383–1392, 2017, doi: 10.1016/j.apenergy.2016.01.003.

[14] M. C. Chiong *et al.*, "Combustion and emission performances of coconut, palm and soybean methyl esters under reacting spray flame conditions," *J. Energy Inst.*, vol. 92, no. 4, pp. 1034–1044, 2019, doi: 10.1016/j.joei.2018.07.003.

[15] A. Ganjehkaviri, M. N. Mohd Jaafar, S. E. Hosseini, and A. B. Musthafa, "Performance evaluation of palm oil-based biodiesel combustion in an oil burner," *Energies*, vol. 9, no. 2, pp. 1–10, 2016, doi: 10.3390/en9020097.

[16] A. Arad, E. Sher, and G. Enden, "Modeling soot formation in diesel-biodiesel flames," *Fuel*, vol. 206, pp. 437–452, 2017, doi: 10.1016/j.fuel.2017.06.024.

[17] A. C. Eloka-Eboka, G. O. Igbum, and F. L. Inambao, "Biodiesel methyl ester production and testing from selected African tropical seed oil feedstocks," *Energy Procedia*, vol. 142, pp. 755–767, 2017, doi: 10.1016/j.egypro.2017.12.123.

[18] C. Chu, Y. Amidpour, N. A. Eaves, and M. J. Thomson, "An experimental and numerical study of the effects of reactant temperatures on soot formation in a coflow diffusion ethylene flame," *Combust. Flame*, vol. 233, p. 111574, 2021, doi: 10.1016/j.combustflame.2021.111574.

[19] A. Khosousi *et al.*, "Experimental and numerical study of soot formation in laminar coflow diffusion flames of gasoline/ethanol blends," *Combust. Flame*, vol. 162, no. 10, pp. 3925–3933, 2015, doi: 10.1016/j.combustflame.2015.07.029.

[20] O. Moussa and Z. Driss, "Numerical Investigation of the Turbulence Models Effect on the Combustion Characteristics in a Non-Premixed Turbulent Flame Methane-Air," *Am. J. Energy Res.*, vol. 5, pp. 85–93, 2017, doi: 10.12691/ajer-5-3-3.

[21] S. Orsino, "GTINDIA2013-3689," pp. 5–10, 2018.

[22] M. D. S. J.Luque, J.B.Jeffries, G.P.Smith, D.R.Crosley, K.T.Walsh, M.B.Long, "CH (A-X) and OH (A-X) Optical Emission in an Axisymmetric Laminar Diffusion Flame," *Combust. Flame*, vol. 122, pp. 172–175, 2000.

[23] L. Tosatto, B. A. V. Bennett, and M. D. Smooke, "Comparison of different DRG-based methods for the skeletal reduction of JP-8 surrogate mechanisms," *Combust. Flame*, vol. 160, no. 9, pp. 1572–1582, 2013, doi: 10.1016/j.combustflame.2013.03.024.

[24] F. Rau, S. Hartl, and C. Hasse, "Numerical and experimental investigation of the laminar burning velocity of biofuels at atmospheric and high-pressure conditions," *Fuel*, vol. 247, no. September 2018, pp. 250–256, 2019, doi: 10.1016/j.fuel.2019.03.024.

[25] J. Y. W. Lai, K. C. Lin, and A. Violi, "Biodiesel combustion: Advances in chemical kinetic modeling," *Prog. Energy Combust. Sci.*, vol. 37, no. 1, pp. 1–14, 2011, doi: 10.1016/j.pecs.2010.03.001.

[26] H. Huang, M. Fairweather, J. F. Griffiths, A. S. Tomlin, and R. B. Brad, "A systematic lumping approach for the reduction of comprehensive kinetic models," *Proc. Combust. Inst.*, vol. 30, no. 1, pp. 1309–1316, 2005, doi: 10.1016/j.proci.2004.08.001.

[27] J. Jeon *et al.*, "Flame temperature distributions of biodiesel fuel in a single-cylinder diesel engine," *Fuel Process. Technol.*, vol. 110, pp. 227–234, 2013, doi: 10.1016/j.fuproc.2012.12.019.

[28] G. Mao, K. Shi, C. Zhang, S. Chen, and P. Wang, "Experimental research on effects of biodiesel fuel combustion flame temperature on NOX formation based on endoscope high-speed photography," *J. Energy Inst.*, vol. 93, no. 4, pp. 1399–1410, Aug. 2020, doi: 10.1016/J.JOEI.2020.01.002.

[29] P. Desgroux, A. Faccinetto, X. Mercier, T. Mouton, D. Aubagnac Karkar, and A. El Bakali, "Comparative study of the soot formation process in a 'nucleation' and a 'sooting' low pressure premixed methane flame," *Combust. Flame*, vol. 184, pp. 153–166, 2017, doi: 10.1016/j.combustflame.2017.05.034.

[30] Z. Wang, L. Li, J. Wang, and R. D. Reitz, "Effect of biodiesel saturation on soot formation in diesel engines," *Fuel*, vol. 175, pp. 240–248, 2016, doi: 10.1016/j.fuel.2016.02.048.

[31] M. M. Maricq, "Coagulation dynamics of fractal-like soot aggregates," *J. Aerosol Sci.*, vol. 38, pp. 141–156, 2007, doi: 10.1016/j.jaerosci.2006.11.004.

[32] D. Hou, L. Pascazio, J. Martin, Y. Zhou, M. Kraft, and X. You, "On the reactive coagulation of incipient soot nanoparticles," *J. Aerosol Sci.*, vol. 159, no. September 2021, p. 105866, 2022, doi: 10.1016/j.jaerosci.2021.105866.

[33] M. Wang, Q. Tang, J. Mei, and X. You, "On the Effective Density of Soot Particles in Premixed Ethylene Flames," *Combust. Flame*, vol. 198, pp. 428–435, 2018, doi: 10.1016/j.combustflame.2018.10.004.

[34] B. J. Xi and B. Zhong, "Soot in Diesel Combustion Systems," *Chem. Eng. Technol.*, vol. 29, no. 6, pp. 665–673, 2006, doi: 10.1002/ceat.200600016.

[35] H. Wang, M. Yao, Z. Yue, M. Jia, and R. D. Reitz, "A reduced toluene reference fuel chemical kinetic mechanism for combustion and polycyclic-aromatic hydrocarbon predictions," *Combust. Flame*, vol. 162, no. 6, pp. 2390–2404, 2015, doi: 10.1016/j.combustflame.2015.02.005.

[36] D. D. Das, W. J. Cannella, C. S. McEnally, C. J. Mueller, and L. D. Pfefferle, "Two-dimensional soot volume fraction measurements in flames doped with large hydrocarbons," *Proc. Combust. Inst.*, vol. 36, no. 1, pp. 871–879, 2017, doi: 10.1016/j.proci.2016.06.047.

[37] M. D. Smooke, M. B. Long, B. C. Connelly, M. B. Colket, and R. J. Hall, "Soot formation in laminar diffusion flames," *Combust. flame*, vol. 143, pp. 613–628, 2005, doi: 10.1016/j.combustflame.2005.08.028.

[38] C. T. Chong *et al.*, "Quantification of carbon particulates produced under open liquid pool and prevaporised flame conditions: Waste cooking oil biodiesel and diesel blends," *Fuel*, vol. 270, no. December 2019, p. 117469, 2020, doi: 10.1016/j.fuel.2020.117469.